S. Majid Abdoli[1]
Sirous Shafiei[1,*]
Amir Raoof[2]
Amanollah Ebadi[1]
Yoones Jafarzadeh[1]
Hamed Aslannejad[2]

Water Flux Reduction in Microfiltration Membranes: A Pore Network Study

A 3D pore network model was developed to simulate the removal of dextran from water. Advanced scanning electron microscopy combined with focused ion beam analysis was used to obtain the sizes of the different pore networks that represent the microscopic structure of a porous membrane. The required input transport parameters for modeling were obtained by performing dynamic experiments on dextran adsorption within the pores of a polysulfone membrane. The simulated flux changes demonstrated a good agreement with the experimental data showing that such a model can be used to study the effects of various parameters during the process. Specifically, the results showed an increase in the applied pressure, decreased membrane thickness, increased pore size, while small sizes of contaminant molecules lead to a rise of the flux passing through the membrane.

Keywords: Flux decline, Membrane fouling, Pore network model, Porous media, Water treatment

Received: March 19, 2018; *revised:* April 13, 2018; *accepted:* May 16, 2018

DOI: 10.1002/ceat.201800130

Supporting Information available online

1 Introduction

Water reclamation is becoming a critical worldwide issue, in particular for developing countries that have a growing demand for water in agriculture and industry [1, 2]. For the production of high quality water, several membrane-based processes including microfiltration, ultrafiltration, and reverse osmosis have been applied [3–7]. A continued problem hindering the wide use of membranes for water-treatment processes is fouling, which hinders flow through the membrane and degrades the membrane's performance [8]. Strategies such as optimization of operational conditions and feed pretreatment may be applied to mitigate the fouling problem [9]. Membrane properties including the membrane material, pore size, hydrophilicity, and surface roughness play a key role in membrane fouling [10–12]. Efforts have been made to improve the antifouling properties of membranes, mostly by introducing new types of membrane [13]. In addition, a numerical tool for the modeling of membranes helped to reduce trial and error to achieve an optimal membrane through understanding the mechanisms contributing to the membrane fouling.

So far, the modeling of membrane processes has often been based on the continuum form of conservation equations [14–16]. When applying these models, the membrane is considered as a continuum domain characterized by its macroscopic transport properties, such as porosity and permeability, and the exact morphology of the membranes, the pore sizes, and the pore connections are neglected [17]. The macroscopic transport properties originate from various pore-scale characteristics. The SEM images of membranes clearly show their complex porous structure. Therefore, an accurate use of macroscopic modeling requires an understanding of the links between these two distinctive scales, that is, the pore scale and the continuum macroscopic scale.

In contrast to continuum methods, pore-scale numerical approaches such as network modeling and lattice Boltzmann represent the pore structures of the porous medium. In a pore network model, the void spaces of porous media are considered as an assemblage of pores and throats. In the simplest case of network modeling, the porous membrane is represented by a bundle of straight cylindrical tubes [18, 19].

Although the pore network has been used widely to examine mass transport and the separation of gaseous mixtures in porous membranes [20–25], to our knowledge, it has not been used to model liquid-phase separation. During membrane separation processes in the liquid phase, fouling of the membrane by contaminants causes problem owing to pore blocking, pore constriction, caking, or a combination of these mechanisms [26]. In complete blockage, particles block pore entrances, the so-called pore-sealing effect. In an intermediate blockage, unlike the complete blockage, a number of particles block the pores, which leaves behind a considerable fraction of the pore space. In pore constriction (i.e., standard blocking), particles accumulate at the wall of the membrane void space, which lowers the pore size to create pore constrictions. When particles

[1]S. Majid Abdoli, Prof. Dr. Sirous Shafiei, Dr. Amanollah Ebadi, Dr. Yoones Jafarzadeh
ssirous@yahoo.com
Faculty of Chemical Engineering, Sahand University of Technology, Tabriz, P.O. Box 51335-1996, Iran.

[2]Dr. Amir Raoof, Hamed Aslannejad
Multiscale Porous Media Laboratory, Department of Earth Science, Utrecht University, Utrecht, 3584 CC, The Netherlands.

accumulate at the external surface of a membrane in the feed side, caking takes place. Although different in the underlying processes responsible, all of these mechanisms prevent flow and reduce the flux through the membrane [27–29].

Based on the blocking mechanisms, various models have been proposed in the literature. Tracy and Davis [30] modeled fouling of polycarbonate microfiltration membranes used for removing bovine serum albumin (BSA) protein by considering several mechanisms. They showed that the slope of the total resistance curve as a function of time changed when the dominant mechanism was varied. Noticeably, they showed that when pore constriction or complete pore blocking were dominant, the curve was concave up and for cake filtration or intermediate blockage it was concave down. Ho and Zydney [31] modeled the protein-fouling microfiltration process by combining pore blockage and cake filtration mechanisms. They found a smooth transition from the pore blockage to cake filtration regime. Consequently, there was no need to explicitly use different mathematical formulations to separately describe these two phenomena. Bolton et al. [26] provided five combined fouling models in constant pressure filtration and constant flow operation. They also derived equations from Darcy's law. Duclos-Orsello et al. [32] modeled a microfiltration membrane by considering both internal and external fouling. Beuscher [33] developed a simplified 2D series of independent layers with a pore-size distribution in each layer as a structure of the membrane to study the retention behavior. In this study, the probability of a particle being captured in a pore smaller than the particle size itself was only dependent on the fraction of pores that were smaller than the particle. The modeling results confirmed the observed behavior of experimental retention data, which showed that the filtration efficiency decreased considerably over time. Zhou et al. [34] developed a model for predicting the flux decline in the filtration process by assuming that both pore blockage and cake formation occur simultaneously. Griffiths et al. [35] used a stochastic simulation approach in a constant pressure filtration process. They assumed that blocking is the same for all the throats and the flux in every tube depended only on the number of particles it had sustained. In their model, the probability of a tube receiving a particle was correlated with the flux through it. Krupp et al. [19] extended the proposed model by Griffiths et al. for more complex particle-tube interactions. In these two studies the structure of the membrane was considered as a bundle of parallel tubes. However, the challenge still remains to determine how the interactions of the membrane structure and the operational conditions influence the flux, which will lead to the optimal membrane.

The objective of this study was to develop a pore-scale model to understand the effect of the filtration process within the membrane. A polysulfone membrane was considered owing to its board application in membrane processes, and dextran-T40 was selected as the target contaminant to be removed from the water phase. In our model, fouling was considered as being due to the adsorption of contaminant at the surface of pores and throats over time. Surface coverage would lead to the reduction of the flux and thus would affect the membrane permeability. This method is most accurate when the contaminant size is smaller than the membrane pore size [36, 37], and for the feed streams with low concentration of contaminants, internal fouling due to adsorption is shown to be the responsible fouling mechanism [38]. In particular, this study aimed to (1) use a 3D pore network for the construction of a membrane structure; (2) validate the modeling predictions against the experimental data for dextran molecules by considering the effect of internal fouling due to the adsorption of contaminants; (3) explore how depressurization may lead to high rates of permeate; (4) examine the effect of the dextran molecule size; (5) investigate the impact of the pore size on the separation of dextran molecules as a contaminant in water; and (6) investigate how the contaminant removal is affected by the thickness of the membrane.

2 Modeling Procedure

In this study, the pore-network modeling approach was used to represent the pore structure of a membrane and the mass transport through it.

2.1 Representation of Membrane Structure Using Pore Network Model

2.1.1 Geometry

A 3D cubic network with spherical pores and cylindrical throats was used in which every pore was connected to six adjacent pores, i.e., the coordination number is 6 for internal pores. Although the real pore structures are more complex (e.g., Raoof and Hassanizadeh [39] developed pore networks with pore coordination numbers up to 26), this type of pore network is the most widely used type. The pore-connectivity distribution is most important for multi-phase flow (often due to phase tapping) and less significant under saturated flow, which is the purpose of this study. Following a comparison of the results with the experimental observations, this assumption will be reconsidered. The pore-size ranges, which control solute mixing and flow, however, were taken form a realistic pore-size distribution.

2.1.2 Characterization of Structure

To assign pore sizes to each pore, a normal distribution function was used:

$$R_{pi} = (R_{max} - R_{min})x_i + R_{min} \quad (1)$$

in which R_{min}[1)] and R_{max} are the minimum and maximum radii of pores and x_i is a random number between zero and one. The radius of each throat was chosen to be equal to the minimum radius of the two adjacent pores connected to it to reach the proper porosity.

1) List of symbols at the end of the paper.

Fig. 1 shows the constructed 3D pore network and two neighboring pores connected using a cylindrical throat on the permeable side of membrane.

2.2 Obtaining Pressure in Each Pore

Initially, all the pores were set to be saturated with the liquid water. By applying mass balance and continuity equations for each pore and applying two pressure boundary conditions at opposite sides of the membrane, the internal distribution of pressure was obtained. Next, the flow rate, f_{ij}, flowing through a given throat ij that connects pore i with pore j, was obtained by:

$$f_{ij} = \frac{\Delta P_{ij}}{R_{ij}}, \quad \text{where } R_{ij} = \frac{8\mu l_{ij}}{\pi r_{ij}^4} \tag{2}$$

in which R_{ij} is the resistance to flow in throat ij ($1/R_{ij}$ represents the conductance of throat ij) and ΔP_{ij} is the pressure difference between two adjacent pores i and j. r_{ij} and l_{ij} are the radius and the length of throat ij, respectively, and μ is the dynamic viscosity of the liquid that flows through throat ij.

For an incompressible liquid phase, the continuity equation can be written as:

$$\sum_j f_{ij} = 0 \tag{3}$$

in which the summation is run for each pore i that is connected to a set of pores indicated by j. Combination of Eqs. (2) and (3) provides a system of algebraic equations:

$$GP = b \tag{4}$$

in which G is a sparse matrix that contains flow conductance, P is a vector that contains unknown pressure values, and b is a known vector containing the effect of boundary conditions. Solution of this system provides pressure values in each pore and the flow in each throat can be calculated from Eq. (2).

2.3 Obtaining Concentration in Each Pore and Throat

To model the mass transport through the porous membrane, mass balance equations should be written for each pore and throat.

For our model the following assumptions were made:

- The free molecular diffusion coefficient (D_0), density (ρ), viscosity (μ), and temperature (T) are constant.
- Mass transport may occur by axial convection and diffusion along throats.
- Fouling occurs owing to the adsorption of contaminants at the walls of pores and throats.

Based on the above-mentioned assumptions, a mass balance for a given pore body i may be written as:

$$V_i \frac{dc_i}{dt} = \sum_{j=1}^{CN} f_{ij} c_{ij} - F_i c_i - \sum_{j=1}^{CN} DA_{ij} \frac{c_i - c_{ij}}{l_{ij}/2} - A_i \frac{ds_i}{dt} \tag{5}$$

in which c_i is the average pore-body mass concentration, c_{ij} is the average throat mass concentration, F_i is the total water flux leaving the pore body (defined in Eq. (6)), V_i is the volume of pore body i, f_{ij} is the flow rate in throat ij, ds_i/dt is the adsorption rate in pore i, D is the effective diffusion coefficient (defined in Eq. (7) similar to that in the literature [40]), CN is the coordination number of pore body i, and A_{ij} and A_i are the cross-sectional area of throat ij and the internal surface of pore i, respectively:

$$F_i = \sum_{j=1}^{CN} f_{ij} \tag{6}$$

$$D = D_0 \left(1 - \frac{r_A}{r_{ij}}\right)^4 \tag{7}$$

$$D_0 = \frac{k_B T}{6\pi\mu r_A} \tag{8}$$

D_0 is the free molecular diffusion coefficient of the species, which is calculated by the Einstein-Stokes equation [41] (Eq. (8)), r_A and r_{ij} are the radius of diffusing species and throat ij, respectively. k_B, T, and μ are the Boltzmann constant, the absolute temperature, and the dynamic viscosity of the liquid, respectively. To obtain the adsorption rate, the equation for adsorbed mass concentration can be defined as:

$$\frac{ds}{dt} = k_a c^{n_1} - k_d s^{n_2} \tag{9}$$

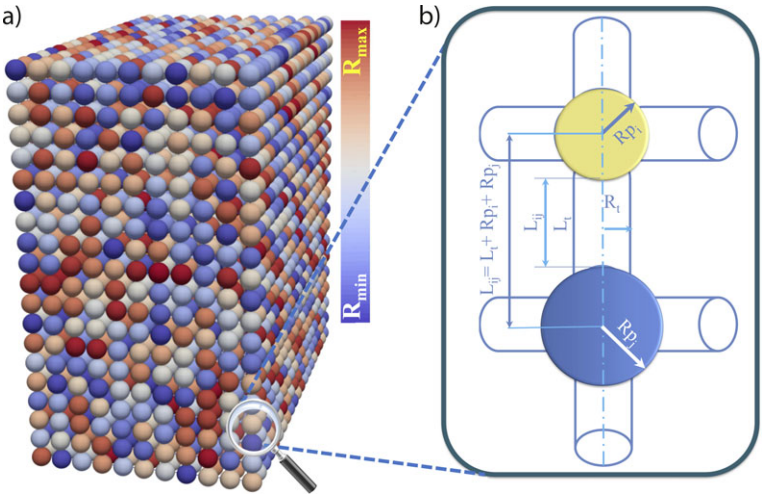

Figure 1. (a) 3D pore network model with different pore sizes; (b) schematic of two neighboring pores connected using a cylindrical throat.

in which s is the average pore-scale concentration in the solid phase, k_a and k_d are the attachment and detachment rate coefficients, respectively, and n_1 and n_2 are constant coefficients. Under equilibrium conditions $ds/dt = 0$, leads to:

$$k_a c^{n_1} - k_d s^{n_2} = 0 \rightarrow s = \left(\frac{k_a}{k_d}\right)^{\frac{1}{n_2}} c^{\frac{n_1}{n_2}} \rightarrow s = Kc^m \tag{10}$$

Eq. (10) is the Freundlich isotherm, which was used in this study to relate the pore-scale concentration and adsorbed concentration at the pore walls. K and m are Freundlich parameters that can be obtained from experimental data. By applying a chain rule to the time derivative of adsorbed mass, we obtained:

$$\frac{ds_i}{dt} = \frac{ds_i}{dc_i}\frac{dc_i}{dt} = Kmc_i^{m-1}\frac{dc_i}{dt} \tag{11}$$

Pore bodies are connected by pore throats. For a given pore throat ij, the mass balance may be written as:

$$V_{ij}\frac{dc_{ij}}{dt} = f_{ij}c_j - f_{ij}c_{ij} - DA_{ij}\frac{c_{ij} - c_i}{l_{ij}/2} - DA_{ij}\frac{c_{ij} - c_j}{l_{ij}/2} - A_{ij}\frac{ds_{ij}}{dt} \tag{12}$$

in which c_j and c_j are the average pore-body mass concentration in pore i and j, respectively; c_{ij} is the average throat mass concentration; V_{ij}, A_{ij}, and l_{ij} are the volume, the cross-sectional area, and the length of throat ij, respectively; f_{ij} is the flow rate in throat ij; D is the effective diffusion coefficient; and ds_{ij}/dt is the adsorption rate in throat ij (defined by Eq. (13)). The first and second terms in the right-hand side of Eq. (12) are convection terms, and the third and fourth terms represent diffusion in throat ij.

$$\frac{ds_{ij}}{dt} = \frac{ds_{ij}}{dc_{ij}}\frac{dc_{ij}}{dt} = Kmc_{ij}^{m-1}\frac{dc_{ij}}{dt} \tag{13}$$

The dextran molecule can be assumed to be spherical and its radius (r_A in meters) can be calculated as [42]:

$$r_A = 0.33\times 10^{-10} MW^{0.46} \tag{14}$$

in which MW is the molar mass in g mol^{-1}.

2.4 Fouling Mechanism

As previously mentioned, three classical fouling mechanisms exist in membrane-filtration processes: pore constriction, pore blockage (complete and intermediate), and cake filtration [28]. Pore constriction is an internal fouling process whereas the other two are external fouling processes. Each process leads to a decline in the flux, and, as a result, decreases the filtration efficiency over time. In this study, internal fouling was considered to be the dominant fouling mechanism owing to the small size of the contaminant molecule relative to the pore sizes, the well-stirred feed side, and the low concentration of the feed. The molecules of diffusing species (i.e., dextran) diffuse in the throats to be possibly adsorbed in the walls of the pore and the throat. The fractional saturation of the active sites is given by using an adsorption isotherm, $S=S(C)$, in which C is the average pore-scale concentration of the contaminant species in the solution phase and S is the average pore-scale concentration in the solid phase. By utilizing the experimental data, the adsorption parameter values $S=4\times10^{-28}C^{10.921}$ (R^2=0.9317) were obtained by curve fitting using the method introduced in Madaeni and Salehi [43]. The thickness of the dynamically adsorbed layer, δ, can be calculated as [44]:

$$\delta^2 - 2R\delta + \frac{8SRr_A}{3} = 0 \tag{15}$$

in which R is the throat or pore radius, r_A is the radius of the diffusing species, and S is the adsorption isotherm. Thus, the radius of the throat or pore after adsorption becomes $R^* = R-\delta$. Therefore, the porosity value is not constant and will decrease during the flow process.

The resistance (R_{ij}) in throat ij defined in Eq. (2) may change with time owing to the increase in the thickness of the adsorbed layer. The modified form of R_{ij} is described as [45]:

$$R_{ij} = \frac{8\mu_l l_{ij}}{\pi r_{ij}^4 \left(1-\varepsilon_{ij}\right)^2} \tag{16}$$

in which ε_{ij} is the volume fraction of the adsorbed layer.

3 Experimental Section

3.1 Materials

For this study, polysulfone (PSf, Udel P-1700 from Solvey) was used as the polymer, together with *N*-methyl-2-pyrrolidone (NMP) and polyethylene glycol (PEG) with a molecular weight of 200 Da from Merck, and dextran (T-40) from Solarbio.

3.2 Preparation of the PSf Membrane

A non-solvent-induced phase separation (NIPS) method was applied to prepare the PSf membrane. The doped solution was prepared by dissolving certain amounts of PSf and PEG in NMP at 60 °C under constant stirring until a homogeneous solution was obtained. The composition of the doped solution was 18 wt % PSf, 10 wt % PEG, and 72 wt % NMP. The homogeneous solution was then allowed to degas overnight. Afterwards, the solution was cast on a glass plate and immediately immersed in distilled water (40 °C) to induce phase separation until the formed membranes were detached freely from the plate. The water bath was refreshed at least three times to complete solvent exchange. Finally, the membrane was dried and stored at 5 °C.

3.3 Imaging of the Membrane

To obtain accurate information on the pore structures, scanning electron microscopy combined with focused ion beam (FIB-SEM) (FEI Company, Eindhoven, Netherlands) was used to slice and image the membrane (see the video in the Supporting Information). By using the obtained images one can use an image analysis method to extract the morphology of the membrane. The pore size and porosity of the membrane was obtained by analyzing the 3D images. A membrane 1 cm^2 was prepared for imaging. First, the sample was sputter-coated with platinum (ca. 8 nm) (HQ280; Cressington Scientific Instruments Ltd, Watford, UK). Then the prepared sample was placed in the vacuum chamber for FIB-SEM. The imaging conditions were set to 2 kV and 21 pA. The FIB acceleration voltage was set to 30 kV for all processes (e.g., deposition, rough cutting, polishing). Detailed information on the FIB-SEM imaging technique can be found in the report by Aslannejad et al. [46]. Fig. 2 shows the SEM image of the surface of the membrane and one layer of the scanned inner structure of the membrane. By reassembling the scanned images of the inner structure of the sample and setting a threshold value, the 3D structure of the material was extracted (Fig. 2 c). Fig. 2 shows the presence of a network of pores and throats from which the pore sizes were extracted as well.

3.4 Membrane Filtration

A membrane filtration experiment was conducted in a self-made dead-end filtration system. Before the filtration test, the pure-water flux through the membrane was measured at a transmembrane pressure of 1.5 bar. The system was then filled with dextran solution (1.0 g L^{-1}) and the flux of the membrane was measured for six hours:

$$J = \frac{M}{At} \tag{17}$$

in which J is the permeate flux (kg $m^{-2}h^{-1}$), M is the collected mass of water (kg), A is the membrane surface area (m^2), and t is time (h).

3.5 Model Validation

To verify the developed model the following procedure was taken. The coefficient of determination (R^2) and mean-squared error (MSE), defined in Eqs. (18) and (19) similarly to that of Hamzehie et al. [47], were used to validate the model with the experimental results.

$$R^2 = \frac{\sum_{i=1}^{n}\left(\alpha_{exp} - \alpha_{avg}\right)^2 - \sum_{i=1}^{n}\left(\alpha_{exp} - \alpha_{mod}\right)^2}{\sum_{i=1}^{n}\left(\alpha_{exp} - \alpha_{avg}\right)^2} \tag{18}$$

$$MSE = \frac{1}{n}\sum_{i=1}^{n}\left(\alpha_{exp} - \alpha_{mod}\right)^2 \tag{19}$$

where α_{exp}, α_{avg}, and α_{mod} are the experimental value, the average of experimental values, and modeling value, respectively.

4 Results and Discussion

For the pore-scale modeling, a domain size of $11\times20\times20$ pores was considered. Such a domain percolates through the whole thickness of the membrane and has sufficient pores in the cross-sectional direction. Simulation parameter values representing the separation of dextran (T-40) have been considered, including T = 25 °C, ΔP = 1.5 bar, and $\mu = 8.9\times10^{-4}$ Pa s. Transport properties of the membrane are provided in Tab. 1.

Table 1. The properties of the membrane.

Membrane type	polysulfone
Mass per sheet [g]	0.031
Porosity [%]	≈ 67
Thickness [μm]	140
Area [cm^2]	4.9
Maximum radius of pore [μm]	6.6
Minimum radius of pore [μm]	4.8

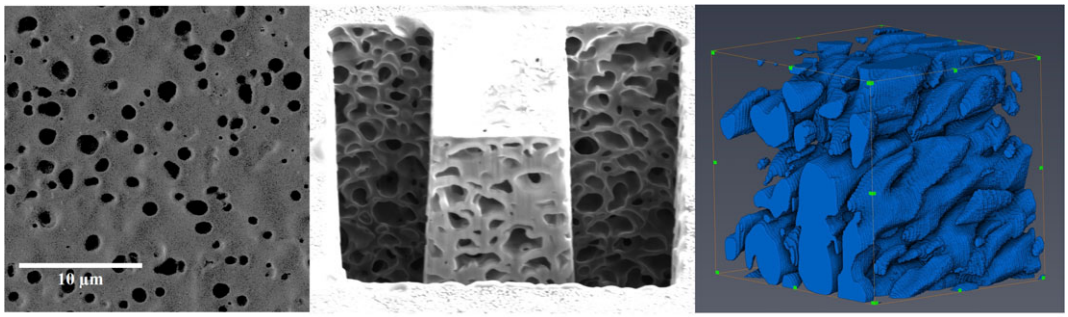

Figure 2. (a) SEM image of the membrane surface; (b) a layer of the inner structure during FIB-SEM imaging; (c) 3D structure obtained by reassembling the successive 2D images.

Initially, at the beginning of the process, no contaminant is present within the membrane pores in the solution phase (i.e., $c(x,0) = 0$). The adsorbed mass is also initially equal to zero (i.e., $s(x,0) = 0$). The boundary conditions used at the inlet, feed side, is $c_0 = 1000$ ppm and that for the outlet face (i.e., at $x = L$) is set to $dc/dx = 0$.

4.1 Flux over Time

To validate the pore-network model, the same domain size and boundary conditions as those used for the experiments were applied to the simulation, and the results were compared with the experimental observations. As the experiment progresses, the adsorption causes shrinkage of the pore spaces, and, consequently, a decrease of the water flux through the membrane. Fig. 3 shows a comparison of the modeling results for the temporal evolution of water flux over time together with the experimental data. A clear decrease in water flux though the pore spaces was observed, which is similar to the experimental data. The maximum discrepancy between the modeling and experimental results are at the initial times. This divergence may partially be due to ignoring the exact morphology of the membrane or the external fouling such as cake formation at the feed side. As shown by FIB-SEM analysis in the previous section, the exact morphology of the membrane structure is complex and considering the void spaces of the membrane as regular pore network may partially affect the results. Moreover, when the membrane is placed in contact with the feed solution, the contaminant may form a cake layer at the membrane surface that affects the resistance to flow through the membrane. Despite this, the modeling results are in good agreement with the experimental data ($R^2 = 0.9055$, $MSE = 0.0024$). After around 50 min, the rate of flux reduction decreases, which indicates the beginning of a quasi-steady-state period. The decrease of the water flux is due to the adsorption of contaminant at the pore walls. Fig. 4 a illustrates the profile of the adsorbed phase along the membrane thickness. To obtain the profiles of Fig. 4 a, the adsorbed mass concentrations were averaged over the pores located at several longitudinal distances over the domain cross-section. Pores near the feed side, due to their higher solution phase concentration, get a larger amount of adsorbed mass. The amount of adsorption increases over time,

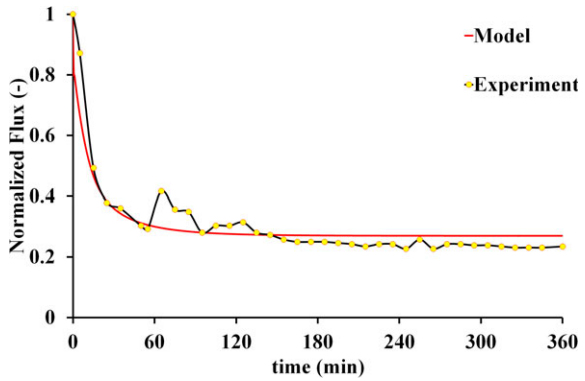

Figure 3. A comparison of the normalized flux of the permeate between the model and experimental data over time.

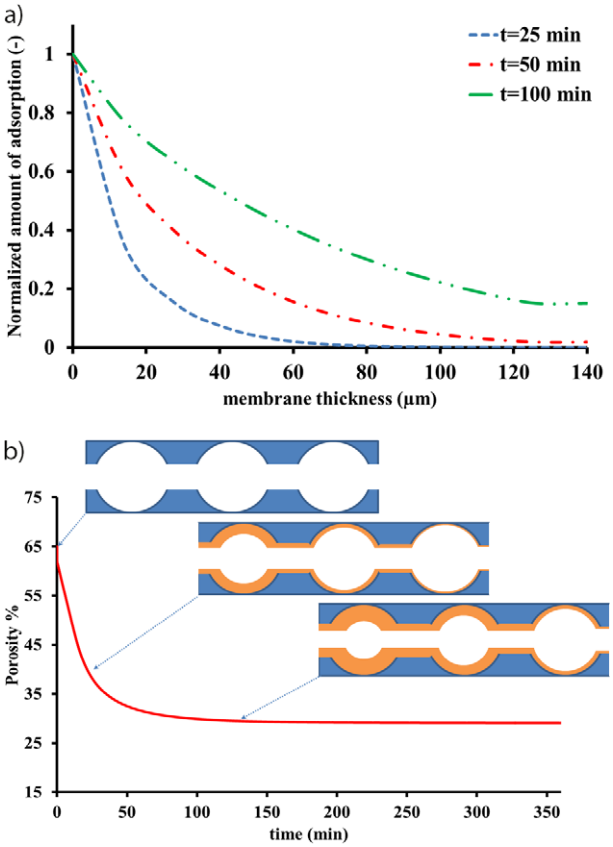

Figure 4. (a) Normalized amount of adsorption versus membrane thickness at three different times; (b) porosity of the membrane over time and a schematic representation of pore constriction.

which causes a decrease of the pore space volume, and therefore porosity, of the medium. The pore scale modeling formulation, in contrast to the continuum scale modeling, allows for tracking of pore volume changes (i.e., porosity) over time, which is important in membrane filtration. Fig. 4 b depicts how the porosity of the membrane decreases during the process time mainly due to the adsorption of contaminants at the membrane.

After the validation of the model, the effects of the applied pressure difference, dextran molecule size, membrane pore size, and membrane thickness were examined. To explore the effect of each of these parameters, at each stage only the parameter under study was varied. In addition, unlike adsorption in the gas phase, adsorption parameters (K and m) are not dependent on pressure in a liquid system. Therefore, they will be considered to be constant in all of the simulations.

4.2 Effect of Applied Pressure Difference

Gradients in the chemical potential, the electrical potential, and the pressure are the driving forces in membrane processes. According to this classification, microfiltration processes similar to ultrafiltration and reverse-osmosis processes are classified as pressure-driven processes [48]. In many microfiltration

applications, the flux of the permeate may vary with operational conditions such as applied pressure. The effect of the applied pressure difference on the permeate flux of was investigated for the range of 1–2 bar. The flux-decline curves exhibited a comparable behavior for three applied pressure differences as shown in Fig. 5. On increasing the applied pressure difference, the permeate flux increased as well. This action led to an increase in the driving force, which was also studied experimentally [49–51]. In practice, the magnitude of the applied pressure difference for the membrane can be varied to obtain an optimum performance.

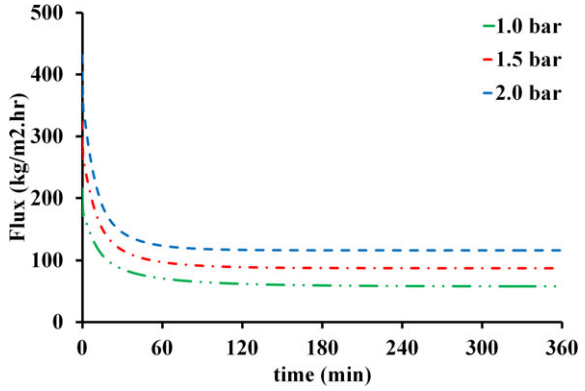

Figure 5. The flux of the permeate over time under different applied pressures.

4.3 Effect of the Molecular Size of Dextran

The effect of the molecular size of the contaminant was investigated for three molecule sizes of dextran (T-10, T-40, T-70). On increasing the molecular weight of the dextran the radius of the contaminant will change (Eq. (14)). Fig. 6 shows the effect of this parameter on the flux and porosity. The size of the molecule affects the diffusivity and the thickness of the adsorbed layer (as explained in Sect. 2) at the wall of pores and throats, and eventually alters the permeate flux. On increasing the molecular size of the contaminant, the resistance rises, and the molecules may not be able to pass through the pores and throats. As a result, the permeate flux will decrease. In addition, the application of larger molecules causes an earlier blockage of the membrane and a decrease of the membrane porosity and flux though it. This trend is consistent with a previous experimental study [52].

4.4 Effect of Pore-Size Distribution

By changing the casting solution composition [53, 54], casting conditions [55], and coagulation bath composition [56], the structure of the membrane (including pore sizes and porosity) can be altered [57]. As discussed in Sect. 2, the normal distribution function is used for pore-size distribution. It is clear that when the maximum and minimum radii are multiplied by a constant number, the mean pore size will be multiplied by the constant number, too. Three pore-size distributions (i.e., three mean pore sizes: 1.2*R*, *R*, and 0.8*R* in which *R* is the mean pore

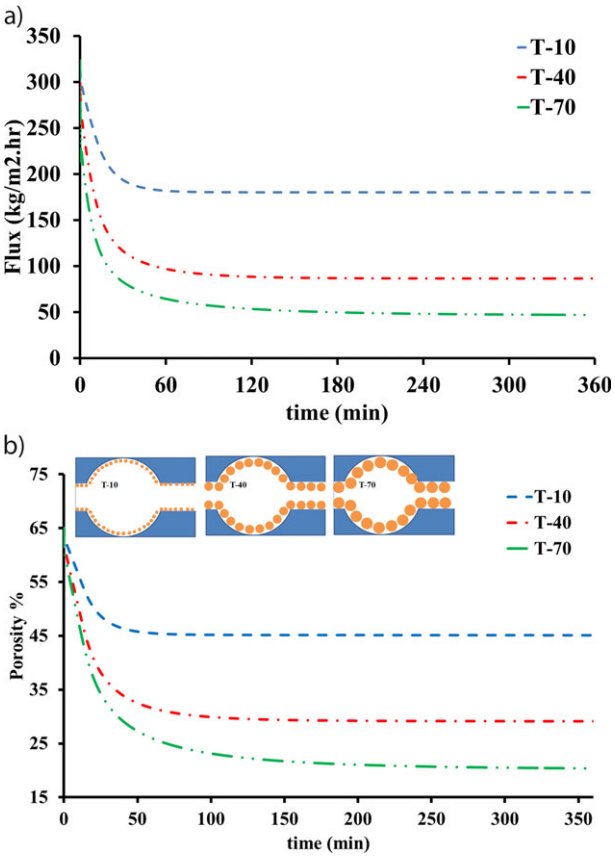

Figure 6. (a) Flux of the permeate; (b) porosity of the membrane over time for different sizes of dextran.

size of the validated model) were considered to study this effect and how it causes a flux reduction. The results are provided in Figs. 7 and 8. As can be seen from Fig. 7, an increase in the pore size of the membrane leads to an increase in the flux as there is more void space for the fluid to pass through the membrane. In contrast, when the pore size of the membrane decreases at a constant molecule size (dextran-T40), the resistance to flow in the membrane increases. This is shown by

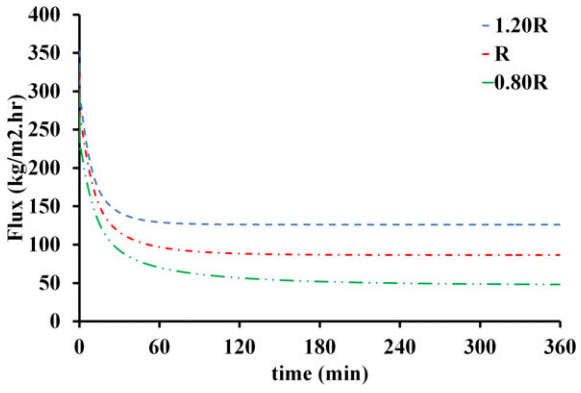

Figure 7. The flux of the permeate over time for different membrane pore sizes (*R* is the mean pore size of the validated model).

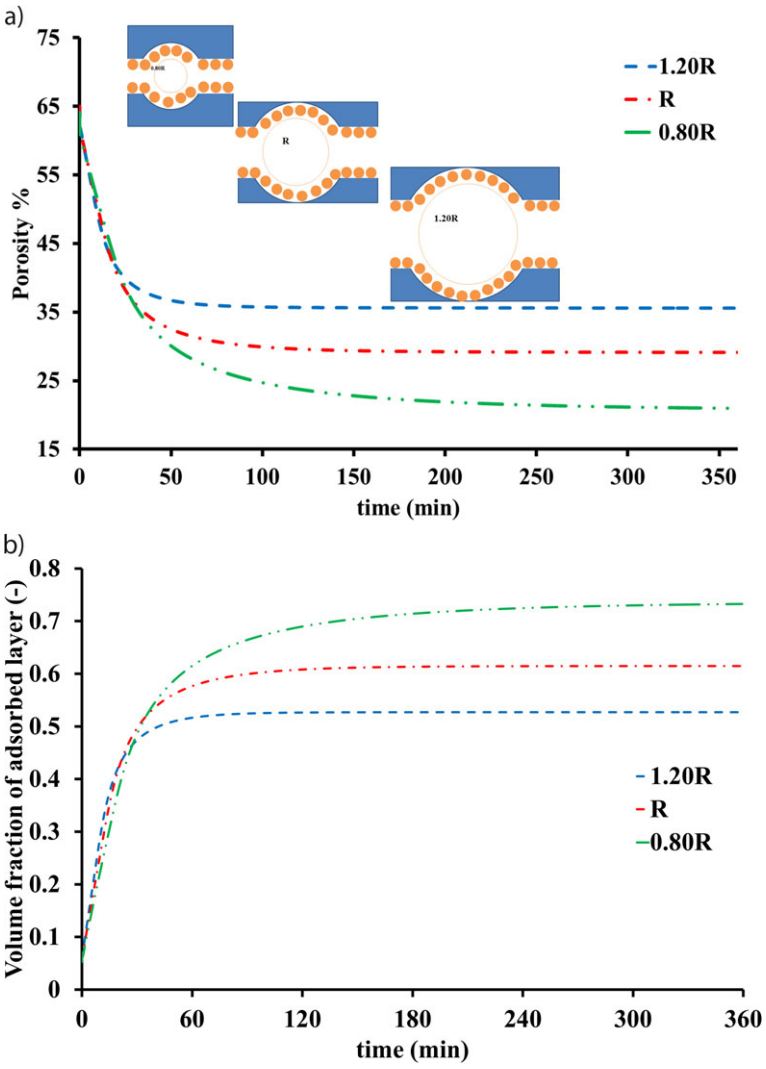

Figure 8. (a) Porosity over time for different membrane pore sizes; b) volume fraction of the adsorbed layer over time.

the flux drop in Fig. 7. This result confirms the fact that the maximum fouling (minimum porosity) can be achieved using a membrane with a pore size close to the diameter of the contaminant particles in the solution to be filtered [29, 49].

The variation of the porosity shows two different behaviors during the process. The porosity in the three different pore sizes is almost the same before 30 minutes and it deviates after this time as shown in Fig. 8 a. The reason for this is explained in Fig. 8 b, in which the average volume fraction of the adsorbed layer in the network over time is shown. As a whole, the thickness of the adsorbed layer increases over time. However, up to a certain point (30 minutes), the volume fraction does not change sufficiently for the three different pore sizes. Consequently, the overall porosity of the membrane will be the same in the three pore sizes. Afterwards, the volume fraction of the adsorbed layer increases by decreasing the pore size. Accordingly, the porosity of the medium will be low at small pore size distributions.

The normalized average concentration, $\bar{c}(x,t)$, is defined as:

$$\bar{c}(x,t) = \frac{1}{c_0}\left[\frac{\sum_{i=1}^{N_t} c_i(x,t)F_i}{\sum_{i=1}^{N_t} F_i}\right] \quad (20)$$

in which c_0 and N_t are the feed concentration and the total number of pore bodies, respectively. The breakthrough curve at the outlet is plotted in Fig. 9. On increasing the mean pore size, the diffusivity of the contaminant and adsorption capacity will be affected. The normalized concentration will increase at the same time and with decreasing mean pore size, the breakthrough curve is widened. This means that decreasing the mean pore size of the membrane delays the time of total saturation.

4.5 Effect of Membrane Thickness

In this step, the cross-sectional area of the membrane and other simulation parameters were kept constant and the thickness of the membrane was modified. Three sizes of membrane were used and the results are shown in Fig. 10. As can be seen in Fig. 10 a, as the membrane thickness increases, owing to the increase in the path length of fluid passing through membrane, the overall resistance of the membrane increases, and, therefore, the permeate flux over time decreases. This trend can also be seen in other studies [58]. In addition, increasing the membrane thickness causes the effective adsorption area to grow. Thus the reduction of porosity in a thicker membrane will be smoother than that of a thinner membrane (Fig. 10 b). Fig. 10 c depicts the effect of the membrane thickness on the breakthrough curve. A thinner membrane, due to low adsorption area, will be saturated sooner.

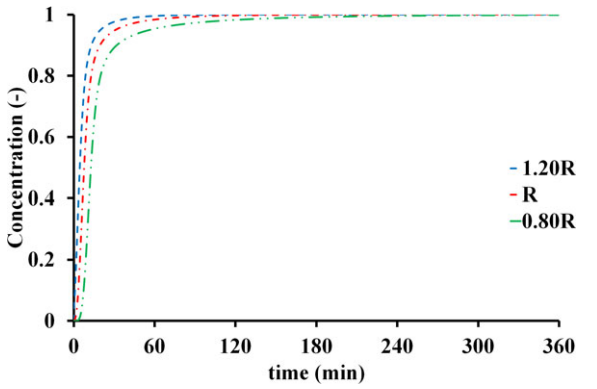

Figure 9. Breakthrough curve at the outlet of the network over time for different pore-size distributions.

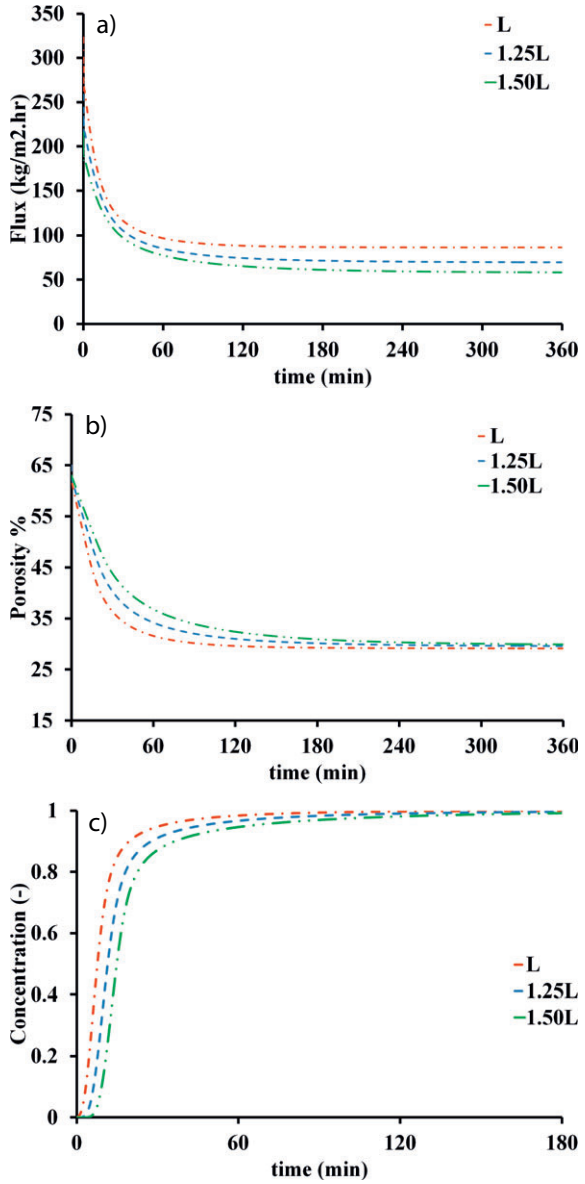

Figure 10. (a) Flux of the permeate, (b) porosity, and (c) breakthrough curve at the outlet of the network over time for different membrane thicknesses.

5 Summary and Conclusion

An understanding of the flux reduction and the ability to predict the membrane performance is essential to improve the water purification efficiency. The flux reduction through the membrane has been studied in the literature. Here, built on the previous studies, we have developed a mechanistic-based quantitative pore-scale model to consider several important operational conditions and the pore structure of the medium.

In this study, a 3D pore-network model was developed to model a polysulfone membrane in the treatment of dextran from water. We assumed internal blocking (i.e., standard blocking or pore constriction) as the dominant mechanism responsible for the adsorption. A remarkable aspect of this work is the use of nonlinear adsorption kinetics, which was numerically applied by using a chain rule. This procedure lowers the number of kinetic parameters to two using the Freundlich equation and lowers the computational time.

Unlike in the continuum-scale models, the porosity was dynamically varied in the pore-scale model based on the calculation of the adsorbed layer. Implementing this model including adsorption and blockage showed a good agreement with the experimental data on the flux reduction. After validation with the experimental observation on flux reduction, the model was used to evaluate the influence of several key parameters including (1) applied pressure difference, (2) dextran molecule size, (3) pore-size distribution, and (4) membrane thickness. Clearly, increasing the applied pressure difference increased the driving force for separation. Increasing the size of the contaminant molecules reduces the permeate flux owing to the blocking and thus decreases the porosity. Pore-size distribution affects the membrane performance. So small pore sizes increase the resistance to flow and reduces the flux. Thin membranes have less resistance to flow. In summary, it may be concluded that the pore-network model has a good agreement with the experimental data and can be utilized for the prediction of membrane fouling during separation processes. Therefore, such a methodology provides hope for performing modeling studies to predict flux reduction behavior before performing experimental studies. In this way, the experimental cost and the associated time can be considerably optimized.

The authors have declared no conflict of interest.

Symbols used

A	[m^2]	membrane surface area
A_i	[m^2]	internal surface of pore i
A_{ij}	[m^2]	cross-section of throat ij
b	[–]	known vector
$\bar{c}$	[–]	normalized average concentration
c_0	[ppm]	feed concentration
c_i	[ppm]	average mass concentration of pore i
c_{ij}	[ppm]	average mass concentration of throat ij
CN	[–]	coordination number of pore body i
D	[m^2s^{-1}]	effective diffusion coefficient
D_0	[m^2s^{-1}]	free molecular diffusion coefficient of the species
f_{ij}	[m^3s^{-1}]	flow rate in throat ij
F_i	[m^3s^{-1}]	total water flux leaving pore body i
G	[m^4kg^{-1}]	sparse matrix that contains flow resistance
J	[$kg\,m^{-2}h^{-1}$]	permeate flux
k_a	[$mg\,g^{-1}ppm^{-n1}$]	attachment rate coefficient
k_B	[$J\,K^{-1}$]	Boltzmann constant
k_d	[$mg^{1-n2}g^{n2-1}$]	detachment rate coefficients
K, m	[–]	Freundlich parameters
l_{ij}	[m]	length of throat ij
M	[kg]	collected mass of water
MW	[$g\,mol^{-1}$]	molar mass

n_1, n_2	[–]	power of adsorbed mass concentration equation
N_t	[–]	total number of pore bodies
P	[Pa]	vector that contains unknown pressure values
ΔP_{ij}	[Pa]	pressure difference between two adjacent pores *i* and *j*
r_A	[m]	radius of diffusing species
r_{ij}	[m]	radius of throat *ij*
R^2	[–]	coefficient of determination
R_{ij}	[m]	resistance to flow in throat *ij*
R_{pi}	[m]	radius of pore *i*
R_{max}	[m]	maximum radius of the pores
R_{min}	[m]	minimum radius of the pores
s_i	[mg g^{-1}]	average concentration in the solid phase of pore *i*
s_{ij}	[mg g^{-1}]	average concentration in the solid phase of throat *ij*
t	[h]	time
T	[K]	absolute temperature
V_i	[m^3]	volume of pore *i*
V_{ij}	[m^3]	volume of throat *ij*
x_i	[–]	a random number between zero and one

Greek letters

α_{avg}	[–]	average of experimental values
α_{exp}	[–]	experimental value
α_{mod}	[–]	modeling value
δ	[m]	thickness of the adsorbed layer
ε_{ij}	[–]	volume fraction of adsorbed layer in throat *ij*
μ	[Pa s]	dynamic viscosity of liquid

Abbreviations

BSA	bovine serum albumin
MSE	mean-squared error
NIPS	non-solvent-induced phase separation
NMP	*N*-methyl-2-pyrrolidone
PEG	polyethylene glycol
PSf	polysulfone

References

[1] D. Mara, *Domestic Wastewater Treatment in Developing Countries*, 1st ed., Routledge, London **2004**.

[2] T. Peters, *Chem. Eng. Technol.* **2010**, *33*, 1233–1240. DOI: 10.1002/ceat.201000139

[3] A. Behboudi, Y. Jafarzadeh, R. Yegani, *Chem. Eng. Res. Des.* **2016**, *114*, 96–107. DOI: 10.1016/j.cherd.2016.07.027

[4] J. Zeng, L. Zheng, X. Sun, Q. He, *Chem. Eng. Technol.* **2011**, *34*, 718–726. DOI: 10.1002/ceat.201000493

[5] T. Coskun, A. Yildirim, C. Balcik, N. Manav Demir, E. Debik, *Clean: Soil, Air, Water* **2013**, *41*, 463–468. DOI: 10.1002/clen.201200075

[6] A. Ullah, R. G. Holdich, M. Naeem, S. W. Khan, V. M. Starov, *Chem. Eng. Res. Des.* **2014**, *92*, 2775–2781. DOI: 10.1016/j.cherd.2014.02.017

[7] A. Ullah, R. G. Holdich, M. Naeem, V. M. Starov, *J. Membr. Sci.* **2012**, *421–422*, 69–74. DOI: 10.1016/j.memsci.2012.06.040

[8] B. Teychene, G. Collet, H. Gallard, *J. Membr. Sci.* **2016**, *505*, 185–193. DOI: 10.1016/j.memsci.2016.01.039

[9] N. Hilal, O. O. Ogunbiyi, N. J. Miles, R. Nigmatullin, *Sep. Sci. Technol.* **2005**, *40*, 1957–2005. DOI: 10.1081/SS-200068409

[10] P. Le-Clech, V. Chen, T. A. G. Fane, *J. Membr. Sci.* **2006**, *284*, 17–53. DOI: 10.1016/j.memsci.2006.08.019

[11] Z. Zhou, S. Rajabzadeh, A. R. Shaikh, Y. Kakihana, W. Ma, H. Matsuyama, *J. Membr. Sci.* **2016**, *514*, 537–546. DOI: 10.1016/j.memsci.2016.05.008

[12] A. Behboudi, Y. Jafarzadeh, R. Yegani, *J. Membr. Sci.* **2017**, *534*, 18–24. DOI: 10.1016/j.memsci.2017.04.011

[13] N. Riyasudheen, M. J. Paul, A. Sujith, *Chem. Eng. Technol.* **2014**, *37*, 1021–1029. DOI: 10.1002/ceat.201300397

[14] S.-Y. Suen, M. R. Etzel, *Chem. Eng. Sci.* **1992**, *47*, 1355–1364. DOI: 10.1016/0009-2509(92)80281-G

[15] W. Shi, F. Zhang, G. Zhang, *J. Chromatogr. A* **2005**, *1081*, 156–162.

[16] C. Boi, S. Dimartino, G. C. Sarti, *J. Chromatogr. A* **2007**, *1162*, 24–33.

[17] A. O. Imdakm, M. Sahimi, *Chem. Eng. Sci.* **1991**, *46*, 1977–1993.

[18] G. Jonsson, *Desalination* **1980**, *35*, 21–38.

[19] A. U. Krupp, I. M. Griffiths, C. P. Please, *Proc. R. Soc. A* **2017**, *473*, 20160948. DOI: 10.1098/rspa.2016.0948

[20] M. Sahimi, T. T. Tsotsis, *Phys. B* **2003**, *338*, 291–297.

[21] A. M. Vieira-Linhares, N. A. Seaton, *Chem. Eng. Sci.* **2003**, *58*, 5251–5256.

[22] F. Chen, R. Mourhatch, T. T. Tsotsis, M. Sahimi, *J. Membr. Sci.* **2008**, *315*, 48–57. DOI: 10.1016/j.memsci.2008.02.005

[23] N. Rajabbeigi, B. Elyassi, T. T. Tsotsis, M. Sahimi, *J. Membr. Sci.* **2009**, *335*, 5–12. DOI: 10.1016/j.memsci.2009.02.033

[24] N. Rajabbeigi, T. T. Tsotsis, M. Sahimi, *J. Membr. Sci.* **2009**, *345*, 323–330.

[25] R. Mourhatch, T. T. Tsotsis, M. Sahimi, *J. Membr. Sci.* **2010**, *356*, 138–146.

[26] G. Bolton, D. LaCasse, R. Kuriyel, *J. Membr. Sci.* **2006**, *277*, 75–84. DOI: 10.1016/j.memsci.2004.12.053

[27] H. P. Grace, *AIChE J.* **1956**, *2*, 307–315. DOI: 10.1002/aic.690020307

[28] J. Hermia, *Trans. Inst. Chem. Eng.* **1982**, *60*, 183–187.

[29] A. Grenier, M. Meireles, P. Aimar, P. Carvin, *Chem. Eng. Res. Des.* **2008**, *86*, 1281–1293. DOI: 10.1016/j.cherd.2008.06.005

[30] E. M. Tracey, R. H. Davis, *J. Colloid Interface Sci.* **1994**, *167*, 104–116. DOI: 10.1006/jcis.1994.1338

[31] C.-C. Ho, A. L. Zydney, *J. Colloid Interface Sci.* **2000**, *232*, 389–399. DOI: 10.1006/jcis.2000.7231

[32] C. Duclos-Orsello, W. Li, C. C. Ho, *J. Membr. Sci.* **2006**, *280*, 856–866. DOI: 10.1016/j.memsci.2006.03.005

[33] U. Beuscher, *Chem. Eng. Technol.* **2010**, *33*, 1377–1381. DOI: 10.1002/ceat.201000123

[34] Y. Zhou, Z. Zhu, Z. Wang, X. Zhang, K. Gao, L. Liu, L. Cheng, *J. Chem. Technol. Biotechnol.* **2016**, *91*, 1082–1092. DOI: 10.1002/jctb.4688

[35] I. M. Griffiths, A. Kumar, P. S. Stewart, *J. Colloid Interface Sci.* **2014**, *432*, 10–18. DOI: 10.1016/j.jcis.2014.06.021

[36] K. Nakamura, K. Matsumoto, *J. Chem. Eng. Jpn.* **1998**, *31*, 536–544.

[37] F. Martinez, A. Martin, P. Pradanos, J. I. Calvo, L. Palacio, A. Hernandez, *J. Colloid Interface Sci.* **2000**, *221*, 254–261.
[38] M. Taniguchi, J. E. Kilduff, G. Belfort, *Environ. Sci. Technol.* **2003**, *37*, 1676–1683.
[39] A. Raoof, S. Majid Hassanizadeh, *Transp. Porous Media* **2010**, *81*, 391–407. DOI: 10.1007/s11242-009-9412-3
[40] L. M. Bryntesson, *J. Chromatogr. A* **2002**, *945*, 103–115. DOI: 10.1016/S0021-9673(01)01485-6
[41] M. Cappelezzo, C. A. Capellari, S. H. Pezzin, L. A. F. Coelho, *J. Chem. Phys.* **2007**, *126 (22)*, 224516. DOI: 10.1063/1.2738063
[42] K. A. Granath, B. E. Kvist, *J. Chromatogr. A* **1967**, *28*, 69–81.
[43] S. S. Madaeni, E. Salehi, *Chem. Eng. J.* **2009**, *150*, 114–121. DOI: 10.1016/j.cej.2008.12.005
[44] Q. Xiong, A. P. Jivkov, J. R. Yates, *Microporous Mesoporous Mater.* **2014**, *185*, 51–60. DOI: 10.1016/j.micromeso.2013.09.038
[45] C. Z. Qin, S. M. Hassanizadeh, *Transp. Porous Media* **2015**, *110*, 345–367. DOI: 10.1007/s11242-015-0546-1
[46] H. Aslannejad, S. M. Hassanizadeh, A. Raoof, D. A. M. de Winter, N. Tomozeiu, M. T. van Genuchten, *Chem. Eng. Sci.* **2017**, *160*, 275–280. DOI: 10.1016/j.ces.2016.11.021
[47] M. E. Hamzehie, S. Mazinani, F. Davardoost, A. Mokhtare, H. Najibi, B. Van der Bruggen, S. Darvishmanesh, *J. Nat. Gas Sci. Eng.* **2014**, *21*, 19–25. DOI: 10.1016/j.jngse.2014.07.022
[48] *Encyclopedia of Membranes* (Eds: E. Drioli, L. Giorno), 1st ed., Springer, Berlin **2016**. DOI: 10.1007/978-3-662-44324-8
[49] S. C. Low, W. X. Jin, M. Tan, *Desalination* **2004**, *167*, 217–226. DOI: 10.1016/j.desal.2004.06.131
[50] K. J. Hwang, C. Y. Liao, K. L. Tung, *Desalination* **2008**, *234*, 16–23. DOI: 10.1016/j.desal.2007.09.065
[51] A. Ullah, V. M. Starov, M. Naeem, R. G. Holdich, *J. Membr. Sci.* **2011**, *382*, 271–277. DOI: 10.1016/j.memsci.2011.08.017
[52] C. F. Lin, Y. J. Huang, O. J. Hao, *Water Res.* **1999**, *33*, 1252–1264. DOI: 10.1016/S0043-1354(98)00322-4
[53] J. Hwang, S. Koo, J. Kim, A. Higuchi, T. Tak, *J. Appl. Polym. Sci.* **1996**, *60*, 1343–1348.
[54] S. S. Madaeni, A. H. Taheri, *Chem. Eng. Technol.* **2011**, *34*, 1328–1334. DOI: 10.1002/ceat.201000177
[55] C. Y. Lai, A. Groth, S. Gray, M. Duke, *Chem. Eng. J.* **2015**, *267*, 73–85. DOI: 10.1016/j.cej.2014.12.036
[56] P. Radovanovic, S. W. Thiel, S. T. Hwang, *J. Membr. Sci.* **1992**, *65*, 213–229. DOI: 10.1016/0376-7388(92)87024-R
[57] I. Kim, K. Lee, *J. Appl. Polym. Sci.* **2003**, *89*, 2562–2566.
[58] C. A. Koval, T. Spontarelli, P. Thoen, R. D. Noble, R. D. Noble, *Ind. Eng. Chem. Res.* **1992**, *31*, 1116–1122. DOI: 10.1021/ie00004a021

